Archives of Civil and Mechanical Engineering (2021) 21:98
https://doi.org/10.1007/s43452-021-00250-2

ORIGINAL ARTICLE

Isogeometric nonlinear bending analysis of porous FG composite microplates with a central cutout modeled by the couple stress continuum quasi-3D plate theory

Rui Rao[1] · Saeid Sahmani[2] · Babak Safaei[3]

Received: 24 April 2021 / Revised: 17 May 2021 / Accepted: 20 May 2021 / Published online: 2 June 2021

Abstract
In the present investigation, by putting the isogeometric finite element methodology to use, the nonlinear flexural response of composite rectangular microplates having functionally graded (FG) porosity is predicted incorporating couple stress type of small scale effect. To accomplish this analysis, a non-uniform kind of rational B-spline functions are employed for an accurate geometrical description of cutouts with various shapes located at the center of microplates. The modified couple stress continuum elasticity is implemented within the framework of a new quasi-three-dimensional (quasi-3D) plate theory incorporating normal deflections with only four variables. By refining the power-law function, the porosity dependency in conjunction with the material gradient are taken into consideration in a simultaneous scheme. The couple stress-based nonlinear flexural curves are achieved numerically based upon a parametrical study. It is demonstrated that for a larger plate deflection, the role of couple stress type of small scale effect on the nonlinear bending curves of porous FG composite microplates is highlighted. It is seen that the gap between nonlinear flexural responses associated with different through-thickness porosity distribution schemes is somehow higher by taking the couple stress effect into account. Also, it is observed that the existence of a cutout at the center of composite microplates makes a change in the slope of their nonlinear flexural curve.

Keywords Couple stress continuum mechanics · Quasi-3D plate model · Isogeometric numerical technique · Small scale effect · Porous composite material

1 Introduction

In recent years, by the progress of material sciences and technologies, a variety of porous systems have been fabricated to produce lightweight and controlled pore structures with favorable functionality and mechanical characteristics. To do so, a great number of research works have been performed. Cheng et al. [1] analyzed the multifaceted capabilities of cellulosic porous structures in health, energy and environment fields. Wang et al. [2] reviewed the electrocatalytic and photocatalytic applications of 2D porous structures. Ansari et al. [3] fabricated porous hollow double-walled Mn_2O_3 cubes capable of enhancing charge diffusion. Zhang et al. [4] fabricated porous structures made of hierarchical carbon material doped with nitrogen atoms through a template free technique to be applied in CO_2 capturing systems. Yu et al. [5] prepared porous carbon structures by utilizing anode component of corn straw using in lithium ion batteries. Lin et al. [6] used graded porous materials to fabricate highly stretchable and ultrasensitive strain sensors having a sandwich structure.

The application of various small-scale effects to classical continuum elasticity is necessary to analyze their effects. To do so, researchers have developed a series of non-classical continuum elasticity theories. Over the last 20 years, a lot of research works have been performed to anticipate size-dependent mechanical features of various small-scaled structural systems. For example, Sahmani and Ansari [7]

✉ Saeid Sahmani
s.sahmani@ug.edu.ge

1 Guangzhou University-Tamkang University Joint Research Centre for Engineering Structure Disaster Prevention and Control, Guangzhou University, Guangzhou 510006, China

2 School of Science and Technology, The University of Georgia, 0171 Tbilisi, Georgia

3 Department of Mechanical Engineering, Eastern Mediterranean University, via Mersin 10, Famagusta, North Cyprus, Turkey

developed different nonlocal models for nonlinear stability analysis of beams at nanoscale using the state-space method. Sahmani et al. [8] indicated the size effect of surface stress on the free oscillations of postbuckled nanobeams. Reddy et al. [9] proposed a nonlocal finite element model for axisymmetric nonlinear bending behavior of circular nanoplates. Togun and Bagdatli [10] analyzed the nonlinear vibrations tensioned Euler–Bernoulli microbeams based on the couple stress theory. Lou et al. [11] investigated couple stress-based plate model for instability analysis of piezoelectric hybrid microplates. Sahmani et al. [12] studied the effect of surface stress on the nonlinear stability of nanoshells under simultaneous axial and radial applied compressive loads. Malikan [13] investigated the couple stress-based shear buckling response of piezoelectric nanoplates under electro-mechanical load. Safaei et al. [14] put the nonlocal continuum elasticity to use for reporting natural frequencies of nanoplates. She et al. [15] incorporated geometrical nonlinearity in bending and buckling characteristics of functionally graded (FG) tubes. Sahmani and Aghdam [16, 17] employed refined truncated cube cell for nonlocal strain gradient bending and forced vibrations of porous microbeams. Arefi et al. [18] constructed a nonlocal sinusoidal shear deformable plate model for free vibrations of FG composite nanoplates. Sahmani and Fattahi [19] explored the nonlocal strain gradient postbuckling of axially loaded FG composite microshells. Soleimani and Tadi Beni [20] derived couple stress-based axisymmetric shell element equations based on a two-node element. Sahmani et al. [21] studied size-dependent nonlinear large deflection of uniformly loaded porous FG composite microbeams using nonlocal strain gradient elasticity.

Recently, Li et al. [22] established a small scale-dependent beam model considering inhomogeneity in conjunction with variation of material properties through-length to explore axially FG nonlocal strain gradient Euler–Bernoulli beams. Sahmani and Aghdam [23] analyzed the axial postbuckling of FG composite microshells based on a nonlocal strain gradient multilayer shell structure. Joshi et al. [24] evaluated effect of thermal environment on the fundamental frequencies of cracked Kirchhoff FG microplates based on strain gradient continuum mechanics. Radic and Jeremic [25] evaluated stability and oscllation responses of inhomogeneous bi-layered graphene nanosheets under hygrothermal loadings according to the differential type of nonlocal continuum mechanics. Using same theory Sahmani and Aghdam [26] analyzed the small scale-dependent instability of cytoplasm-embedded microtubules. Khakalo et al. [27] modeled strain gradient flexural, vibration and buckling of Euler–Bernoulli and Timoshenko microscaled beams made of 2D triangular multilayer composites. Al-Shujairi et al. [28] developed a nonlocal strain gradient continuum beam formulation to evaluate the free oscillations and buckling of FG multilayer microscaled beams by considering thermal conditions. Ruocco et al. [29] established Hencky bar net scheme to investigate the oscillations and buckling of nonlocal axially FG beams at nanoscale. Jia et al. [30] studied the electro-thermo-mechanical stability behaviors of FG composite beams at microscale based upon the couple stress-based continuum mechanics. Taati [31] studied the nonlinear stability behaviors of FG multilayer microbeams incorporating the couple stress size effect.

Ghorbani Shenas et al. [32] explored the thermal postbuckling and prebuckling of pre-twisted rotating FG composite beams at microscale under high temperature variation according to modified strain gradient continuum elasticity. Sarafraz et al. [33] evaluated superharmonic subharmonic and excited nanobeam resonances taking into account the effect of surface stress. Aria and Friswell [34] studied hygro-thermal buckling and vibration responses of FG multilayer temperature-dependent beams at microscale. Jun et al. [35] incorporated three characteristic lengths to the nonlocal continuum mechanics to study the buckling behaviors of nanobeams. Thai et al. [36] established a numerical solution to explore the effect of strain gradient size dependency in free vibrations of FG composite multilayer microplates. Sahmani and Safaei [37] evaluated nonlinear oscillations resonance of bi-directional FG composite microbeams according to nonlocal strain gradient elasticity. Fang et al. [38] developed a novel nonlocal beam model in the absence of shear deformation to examine the thermal buckling and vibrations of FG composite nanobeams under thermal conditions. Sarthak et al. [39] investigated the dynamic stability of curved nanoscaled beams using both third-order shear deformable plate formulation and nonlinear nonlocal finite element method. Yuan et al. [40] studied the nonlinear stability stiffness of FG composite conical microshells by incorporating different size-dependent continuum models. Thai et al. [41] established a size-dependent meshfree numerical model for the analysis of the vibration and deformation behaviors of FG carbon nanotube-reinforced nanobeams. Yuan et al. [42] and Fan et al. [43] predicted the effects of nonlocal and surface stress on FG composite nanoplate shear buckling behaviors, respectively. Zhang et al. [44] applied the finite element technique using a strain gradient higher-order shear flexible beam element to perform dynamic and static analyses on microbeam structures. Daghigh et al. [45] introduced a nonlocal continuum plate formulation to study the buckling and nonlinear bending properties of nanocomposite plates at the nanoscale. Karamanli and Vo [46] studied the free vibrations, buckling and bending of FG multilayer microbeams with the aid of improved strain gradient continuum mechanics. Guo et al. [47] calculated the 3D nonlocal critical stability loads of multilayer nanoplates containing integrated with quasicrystal-free surface layers. Mao et al. [48] evaluated FG piezoelectric composite microplate free vibrations based on nonlocal continuum elasticity. Fan et al. [49] predicted geometrically nonlinear oscillations of porous FG plates through isogeometric analyses. Sahmani and Safaei [50] explored FG composite conical nanoshell large-amplitude vibrations taking into account surface stress effect.

Herein, through combination of the modified couple stress continuum mechanics and a hybrid-type quasi-3D model of plate, the geometrical nonlinear flexural characteristics of porous FG composite microplates are investigated through an accurate description of cutouts having various shapes located at the center of microplates. By employing a porosity-dependent homogenization model, a refined approximation of the material properties of microplates are obtained for each pattern of the through-thickness porosity distribution. By performing a parametrical study, the influences of different parameters on the microstructural-dependent nonlinear flexural response of porous FG composite microplates are monitored.

2 Quasi-3D couple stress-based modelling of porous FG plate

In the current exploration, porous FG composite rectangular microplates in the presence and absence of a central cutout are supposed. Accordingly, the through-thickness porosity distribution is considered in three different patterns as demonstrated in Fig. 1. To have a refined approximation of the material properties including the porous-dependency and material gradient simultaneously, it is assumed as [51]

$$\mathcal{P}(z) = \mathcal{P}_c\left[(1/2 + z/k)^k - \Gamma/2\right] + \mathcal{P}_m\left[1 - (1/2 + z/h)^k - \Gamma/2\right] \tag{1}$$

where Γ denotes the porosity coefficient (index), and k is the index of material gradient.

In accordance with the refined approximation rule, the effective values of Poisson's ratio (ν) and Young's modulus (E) associated with the porous FG composite microplates can be estimated for different schemes of the through-thickness porosity distribution as below

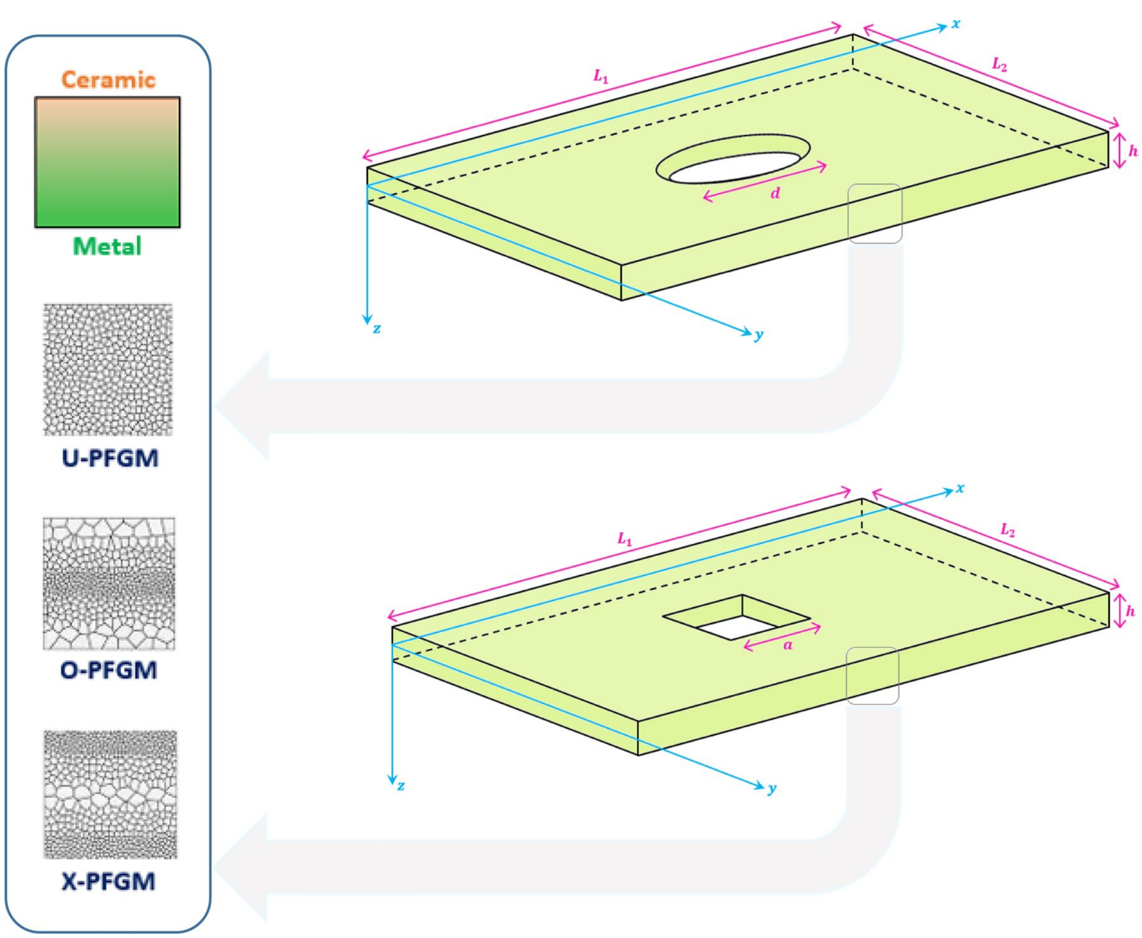

Fig. 1 Representation schematically a porous FG composite microplates having square and circular central located cutouts

$$E(z) = \left(E_c - E_m\right)\varphi_1(z) + E_m - \left(E_c + E_m\right)\Gamma\varphi_2(z) \tag{2a}$$

$$v(z) = \left(v_c - v_m\right)\varphi_1(z) + E_m - \left(v_c + v_m\right)\Gamma\varphi_2(z) \tag{2b}$$

where

$$\varphi_1(z) = (1/2 + z/h)^k, \varphi_2(z) = \begin{cases} 1/2U - PFGM \\ 1/2 - |z|/hO - PFGM \\ -|z|/hX - PFGM \end{cases} \tag{3}$$

The refined approximated Young's modulus is varied with the thickness as well as the porosity index of porous FG composite microplates. The dimensionless form $(E(z)/E_c)$ of these variations are plotted in Figs. 2, 3, 4 relevant to various material gradient indexes.

By separating the transverse plate deflection into the shear components and bending, the components of the quasi-3D displacement vector can be defined. In addition, using a transverse normal shape function to implement the normal deformations along the plate thickness, it yields

$$\mathcal{U}_x(x,y,z) = u(x,y) - zw_{b,x}(x,y) + (\mathbb{f}(z) - z)w_{s,x}(x,y) \tag{4a}$$

$$\mathcal{U}_y(x,y,z) = v(x,y) - zw_{b,y}(x,y) + (\mathbb{f}(z) - z)w_{s,y}(x,y) \tag{4b}$$

$$\mathcal{U}_z(x,y,z) = w_b(x,y) + (1 + \mathbb{g}(z))w_s(x,y) \tag{4c}$$

where $u(x,y)$, $v(x,y)$ in order are the variables of mid-plane deformation along x-axis and y-axis, and $w_b(x,y)$ and $w_s(x,y)$ stand for the bending and shear variables of deformation, respectively. Moreover, the shear deformations as well as the through-thickness normal strains are implemented via the transverse and normal shape functions of $\mathbb{f}(z)$ and $\mathbb{g}(z)$, which are related to $\mathbb{F}(z)$ and $\mathbb{G}(z)$ in the following forms

$$\mathbb{F}(z) = \mathbb{f}(z) - z = \sin(\pi z/h) - z \tag{5a}$$

$$\mathbb{G}(z) = 1 + \mathbb{g}(z) = 1 + (5/12\pi)\cos(\pi z/h)] \tag{5b}$$

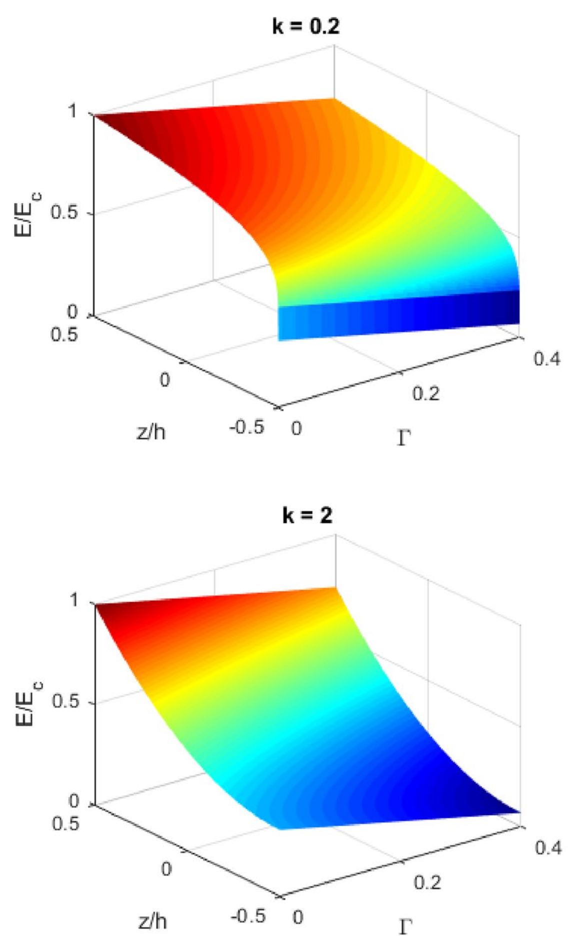

Fig. 2 Dimensionless through-thickness variation of Young's modulus of a porous FG composite microplate having various material gradient indexes (U-PFGM pattern)

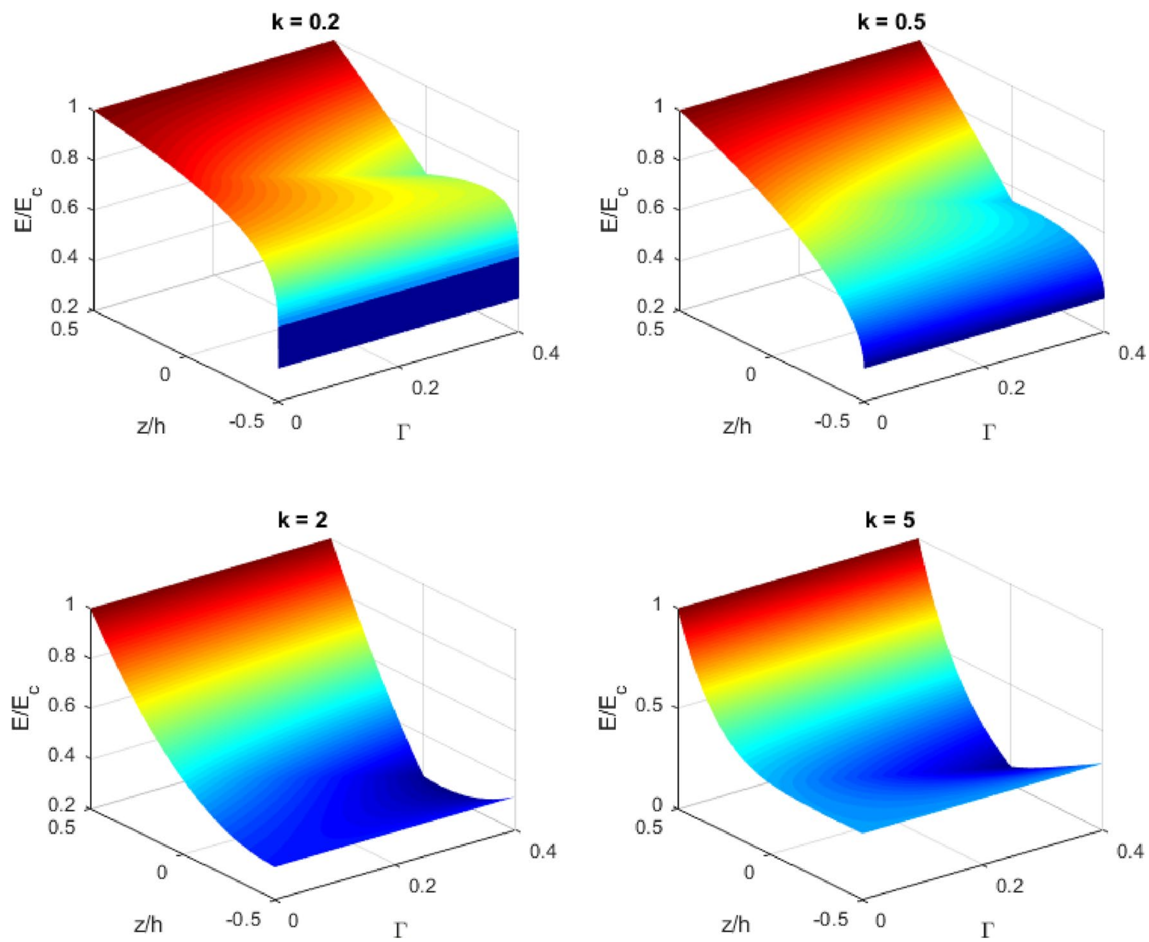

Fig. 3 Dimensionless through-thickness variation of Young's modulus of a porous FG composite microplate having various material gradient indexes (O-PFGM pattern)

In contrast to the first-order shear flexible formulations, the present hybrid quasi-3D plate model has the capability to satisfy the C^0-continuuity requirement without any shear-locking problem. Also, using the trigonometric normal shape function, the through-thickness displacement can be accounted accurately and independently with the transverse shear function.

So, in the presence of nonlinearity in the von-Karman form, the components of the classical strain tensor in terms of the developed quasi-3D displacement field can be achieved as below

$$\varepsilon_{xx} = u_{,x} + \left(w_{b,x} + w_{s,x}\right)^2/2 - zw_{b,xx} + \mathbb{F}(z)w_{s,xx}$$

$$\varepsilon_{yy} = v_{,y} + \left(w_{b,y} + w_{s,y}\right)^2/2 - zw_{b,yy} + \mathbb{F}(z)w_{s,yy}$$

$$\varepsilon_{zz} = \mathbb{G}_{,z}(z)w_s$$

$$\gamma_{xy} = u_{,y} + v_{,x} + \left(w_{b,x} + w_{s,x}\right)\left(w_{b,y} + w_{s,y}\right) - 2zw_{b,xy} + 2\mathbb{F}(z)w_{s,xy} \tag{6}$$

$$\gamma_{xz} = \left(\mathbb{F}_{,z}(z) + \mathbb{G}(z)\right)w_{s,x}$$

$$\gamma_{yz} = \left(\mathbb{F}_{,z}(z) + \mathbb{G}(z)\right)w_{s,y}$$

Thereafter, the constitutive relationships between components of the classical stress and strain tensors can be given as

$$\begin{Bmatrix} \sigma_{xx} \\ \sigma_{yy} \\ \sigma_{zz} \\ \tau_{xy} \\ \tau_{yz} \\ \tau_{xz} \end{Bmatrix} = \begin{bmatrix} Q_{11}(z) & Q_{12}(z) & Q_{13}(z) & 0 & 0 & 0 \\ Q_{12}(z) & Q_{22}(z) & Q_{23}(z) & 0 & 0 & 0 \\ Q_{13}(z) & Q_{23}(z) & Q_{33}(z) & 0 & 0 & 0 \\ 0 & 0 & 0 & Q_{44}(z) & 0 & 0 \\ 0 & 0 & 0 & 0 & Q_{55}(z) & 0 \\ 0 & 0 & 0 & 0 & 0 & Q_{66}(z) \end{bmatrix} \begin{Bmatrix} \varepsilon_{xx} \\ \varepsilon_{yy} \\ \varepsilon_{zz} \\ \gamma_{xy} \\ \gamma_{yz} \\ \gamma_{xz} \end{Bmatrix} \tag{7}$$

where

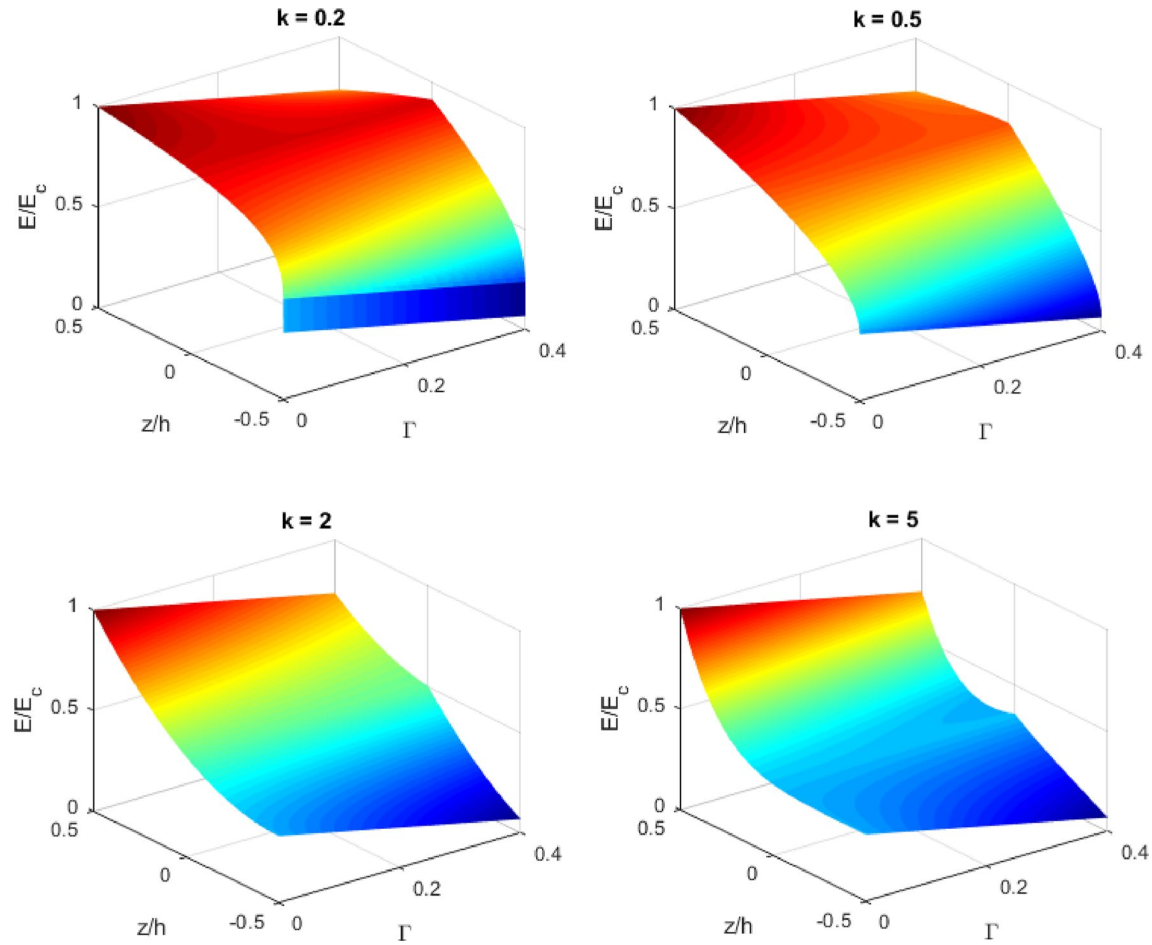

Fig. 4 Dimensionless through-thickness variation of Young's modulus of a porous FG composite microplate having various material gradient indexes (X-PFGM pattern)

$$
\begin{aligned}
Q_{11}(z) &= Q_{22}(z) = Q_{33}(z) = \frac{(1-\nu(z))E(z)}{(1-2\nu(z))(1+\nu(z))}\\
Q_{12}(z) &= Q_{13}(z) = Q_{23}(z) = \frac{\nu(z)E(z)}{(1-2\nu(z))(1+\nu(z))}\\
Q_{44}(z) &= Q_{55}(z) = Q_{66}(z) = \frac{E(z)}{2(1+\nu(z))}
\end{aligned}
\tag{8}
$$

Within the framework of the modified couple stress elasticity of mechanics [52], the rotation gradient tensor can be obtained as follows

$$
\boldsymbol{\chi} = \left[\nabla\boldsymbol{\theta} + (\nabla\boldsymbol{\theta})^T\right]/2 \tag{9}
$$

where the components of the rotation vector can be given as below

$$
\begin{aligned}
\boldsymbol{\theta} &= \begin{Bmatrix} \theta_x \\ \theta_y \\ \theta_z \end{Bmatrix} = \begin{Bmatrix} \left(\mathcal{U}_{z,y} - \mathcal{U}_{y,z}\right)/2 \\ \left(\mathcal{U}_{x,z} - \mathcal{U}_{z,x}\right)/2 \\ \left(\mathcal{U}_{y,x} - \mathcal{U}_{x,y}\right)/2 \end{Bmatrix}\\
&= \begin{Bmatrix} \left[2w_{b,y} + \left(\mathbb{G}(z) - \mathbb{F}_{,z}(z)\right)w_{s,y}\right]/2 \\ \left[-2w_{b,x} - \left(\mathbb{G}(z) - \mathbb{F}_{,z}(z)\right)w_{s,x}\right]/2 \\ \left[v_{,x} - u_{,y}\right]/2 \end{Bmatrix}
\end{aligned}
\tag{10}
$$

By inserting Eq. (4) in Eq. (10), the components of the rotation gradient tensor are achieved as below

$$
\begin{aligned}
\chi_{xx} &= \theta_{x,x} = \left[2w_{b,xy} + \left(\mathbb{G}(z) - \mathbb{F}_{,z}(z)\right)w_{s,xy}\right]/2\\
\chi_{yy} &= \theta_{y,y} = \left[-2w_{b,xy} - \left(\mathbb{G}(z) - \mathbb{F}_{,z}(z)\right)w_{s,xy}\right]/2\\
\chi_{xy} &= \theta_{x,y} + \theta_{y,x}\\
&= \left[w_{b,yy} - w_{b,xx} + \left(\mathbb{G}(z)/2 - \mathbb{F}_{,z}(z)/2\right)\left(w_{s,yy} - w_{s,xx}\right)\right]/2
\end{aligned}
\tag{11}
$$

$$\chi_{xy} = \theta_{x,z} + \theta_{z,x} = \left[v_{,xx} - u_{,xy} + \left(\mathbb{G}_{,z}(z) - \mathbb{F}_{,zz}(z)\right)w_{s,y}\right]/4$$

$$\chi_{yz} = \theta_{y,z} + \theta_{z,y} = \left[v_{,xy} - u_{,yy} - \left(\mathbb{G}_{,z}(z) - \mathbb{F}_{,zz}(z)\right)w_{s,x}\right]/4$$

$$\chi_{zz} = \theta_{z,z} = 0$$

Consequently, the non-classical constitutive relationships between components of the rotation stress tensor and rotation gradient tensor can be presented as

$$\begin{Bmatrix} \Updownarrow_{xx} \\ \Updownarrow_{yy} \\ \Updownarrow_{xy} \\ \Updownarrow_{yz} \\ \Updownarrow_{xz} \end{Bmatrix} = \begin{bmatrix} \frac{l^2E(z)}{1+\nu(z)} & 0 & 0 & 0 & 0 \\ 0 & \frac{l^2E(z)}{1+\nu(z)} & 0 & 0 & 0 \\ 0 & 0 & \frac{l^2E(z)}{1+\nu(z)} & 0 & 0 \\ 0 & 0 & 0 & \frac{l^2E(z)}{1+\nu(z)} & 0 \\ 0 & 0 & 0 & 0 & \frac{l^2E(z)}{1+\nu(z)} \end{bmatrix} \begin{Bmatrix} \chi_{xx} \\ \chi_{yy} \\ \chi_{xy} \\ \chi_{yz} \\ \chi_{xz} \end{Bmatrix} \tag{12}$$

where l represents the internal length scale parameter.

Therefore, the expression associated with the couple stress-based strain energy variation of a porous FG composite microplate modeled includes two separate parts of the classical and non-classical ones in the following form

$$\delta\Pi_C = \int_S \int_{-\frac{h}{2}}^{\frac{h}{2}} \left\{\sigma_{xx}\delta\varepsilon_{xx} + \sigma_{yy}\delta\varepsilon_{yy} + \sigma_{zz}\delta\varepsilon_{zz} + \tau_{xy}\delta\gamma_{xy} + \tau_{yz}\delta\gamma_{yz} + \tau_{xz}\delta\gamma_{xz}\right\} dz dS \tag{13a}$$

$$\delta\Pi_{NC} = \int_S \int_{-\frac{h}{2}}^{\frac{h}{2}} \left\{\Updownarrow_{xx}\delta\chi_{xx} + \Updownarrow_{yy}\delta\chi_{yy} + \Updownarrow_{xy}\delta\chi_{xy} + \Updownarrow_{yz}\delta\chi_{yz} + \Updownarrow_{xz}\delta\chi_{xz}\right\} dz dS \tag{13b}$$

In addition, the applied distributed load $\amalg$ induces a virtual work as below

$$\delta\Pi_W = \int_S \amalg \delta w dS \tag{14}$$

Via employing the variational rules, and inserting Eqs. (7) and (12) in Eq. (13), one will have

$$\int_S \left\{\delta\left(\mathfrak{P}_b^T\right)\boldsymbol{\xi}_b\mathfrak{P}_b + \delta\left(\mathfrak{P}_s^T\right)\boldsymbol{\xi}_s\mathfrak{P}_s + \delta\left(\mathfrak{R}_b^T\right)\boldsymbol{\vartheta}_b\boldsymbol{\Phi}_1\mathfrak{R}_b + \delta\left(\mathfrak{R}_s^T\right)\boldsymbol{\vartheta}_s\mathfrak{R}_s + \amalg\right\} dS = 0 \tag{15}$$

in which

$$\mathfrak{P}_b = \begin{bmatrix} u_{,x} + \left(w_{b,x} + w_{s,x}\right)^2/2 & -w_{b,xx} & w_{s,xx} & 0 \\ v_{,y} + \left(w_{b,y} + w_{s,y}\right)^2/2 & -w_{b,yy} & w_{s,yy} & 0 \\ u_{,y} + v_{,x} + \left(w_{b,x} + w_{s,x}\right)\left(w_{b,y} + w_{s,y}\right) & -2w_{b,xy} & 2w_{s,xy} & 0 \\ 0 & 0 & 0 & w_s \end{bmatrix}^T$$

$$\left\{\mathbf{A_b}, \mathbf{B_b}, \mathbf{C_b}\right\} = \int_{-\frac{h}{2}}^{\frac{h}{2}} \{1, z, \mathbb{F}(z)\} \begin{bmatrix} Q_{11}(z) & Q_{12}(z) & 0 & Q_{13}(z) \\ Q_{12}(z) & Q_{22}(z) & 0 & Q_{23}(z) \\ 0 & 0 & Q_{66}(z) & 0 \\ Q_{31}(z) & Q_{32}(z) & 0 & Q_{33}(z) \end{bmatrix} dz$$

$$\boldsymbol{\xi}_{b16} = \begin{bmatrix} \mathbf{A_b} & \mathbf{B_b} & \mathbf{C_b} & \mathbf{E_b} \\ \mathbf{B_b} & \mathbf{D_b} & \mathbf{F_b} & \mathbf{G_b} \\ \mathbf{C_b} & \mathbf{F_b} & \mathbf{H_b} & \mathbf{K_b} \\ \mathbf{E_b} & \mathbf{G_b} & \mathbf{K_b} & \mathbf{J_b} \end{bmatrix}, \mathfrak{P}_s = \begin{bmatrix} w_{s,x} \\ w_{s,y} \end{bmatrix},$$

$$\boldsymbol{\xi}_s = \int_{-\frac{h}{2}}^{\frac{h}{2}} \left(\mathbb{F}_{,z}(z) + \mathbb{G}(z)\right)^2 \begin{bmatrix} Q_{44}(z) & 0 \\ 0 & Q_{55}(z) \end{bmatrix} dz$$

$$\mathfrak{R}_b = \begin{bmatrix} w_{b,xy} & -w_{s,xy}/2 & w_{s,xy}/2 \\ -w_{b,xy} & w_{s,xy}/2 & -w_{s,xy}/2 \\ \left(w_{b,yy} - w_{b,xx}\right)/2 & -\left(w_{s,yy} - w_{s,xx}\right)/4 & \left(w_{s,yy} - w_{s,xx}\right)/4 \end{bmatrix} \tag{16}$$

$$\boldsymbol{\vartheta}_b = \begin{bmatrix} \mathcal{A}_b & \mathcal{B}_b & \mathcal{E}_b \\ \mathcal{B}_b & \mathcal{D}_b & \mathcal{F}_b \\ \mathcal{E}_b & \mathcal{F}_b & \mathcal{H}_b \end{bmatrix}, \boldsymbol{\Phi}_1 = \begin{bmatrix} \boldsymbol{\varphi}_1 & 0 & 0 \\ 0 & \boldsymbol{\varphi}_1 & 0 \\ 0 & 0 & \boldsymbol{\varphi}_1 \end{bmatrix}, \varphi_1 = \begin{bmatrix} 1 & 0 & 0 \\ 0 & 1 & 0 \\ 0 & 0 & 2 \end{bmatrix}$$

$$\mathfrak{R}_s = \begin{bmatrix} \left(v_{,xx} - u_{,xy}\right)/4 & -w_{s,y}/4 & w_{s,y}/4 \\ \left(v_{,xy} - u_{,yy}\right)/4 & w_{s,x}/4 & w_{s,x}/4 \end{bmatrix}$$

$$\boldsymbol{\vartheta}_s = \begin{bmatrix} \mathcal{A}_s & \mathcal{B}_s & \mathcal{E}_s \\ \mathcal{B}_s & \mathcal{D}_s & \mathcal{F}_s \\ \mathcal{E}_s & \mathcal{F}_s & \mathcal{H}_s \end{bmatrix}, \boldsymbol{\Phi}_2 = \begin{bmatrix} \boldsymbol{\varphi}_2 & 0 & 0 \\ 0 & \boldsymbol{\varphi}_2 & 0 \\ 0 & 0 & \boldsymbol{\varphi}_2 \end{bmatrix}, \varphi_2 = \begin{bmatrix} 2 & 0 \\ 0 & 2 \end{bmatrix}$$

where

$$\left\{\mathbf{D_b},\mathbf{E_b},\mathbf{F_b},\mathbf{G_b}\right\}=\int_{-\frac{h}{2}}^{\frac{h}{2}}\left\{z^2,\mathbb{G}_{,z}(z),z\mathbb{F}(z),z\mathbb{G}_{,z}(z)\right\}\times\begin{bmatrix}Q_{11}(z)&Q_{12}(z)&0&Q_{13}(z)\\Q_{12}(z)&Q_{22}(z)&0&Q_{23}(z)\\0&0&Q_{66}(z)&0\\Q_{31}(z)&Q_{32}(z)&0&Q_{33}(z)\end{bmatrix}dz$$

$$\left\{\mathbf{H_b},\mathbf{K_b},\mathbf{J}_b\right\}=\int_{-\frac{h}{2}}^{\frac{h}{2}}\left\{\mathbb{F}^2(z),\mathbb{F}(z)\mathbb{G}_{,z}(z),\left(\mathbb{G}_{,z}(z)\right)^2\right\}\times\begin{bmatrix}Q_{11}(z)&Q_{12}(z)&0&Q_{13}(z)\\Q_{12}(z)&Q_{22}(z)&0&Q_{23}(z)\\0&0&Q_{66}(z)&0\\Q_{31}(z)&Q_{32}(z)&0&Q_{33}(z)\end{bmatrix}dz$$

$$\left\{\mathcal{A}_b,\mathcal{B}_b,\mathcal{D}_b\right\}=\int_{-\frac{h}{2}}^{\frac{h}{2}}\left\{1,\mathbb{F}_{,z}(z),\left(\mathbb{F}_{,z}(z)\right)^2\right\}\begin{bmatrix}\frac{l^2E(z)}{1+\nu(z)}&0&0\\0&\frac{l^2E(z)}{1+\nu(z)}&0\\0&0&\frac{l^2E(z)}{1+\nu(z)}\end{bmatrix}dz$$

$$\left\{\mathcal{E}_b,\mathcal{F}_b,\mathcal{H}_b\right\}=\int_{-\frac{h}{2}}^{\frac{h}{2}}\left\{\mathbb{G}(z),\mathbb{G}(z)\mathbb{F}_{,z}(z),\mathbb{G}^2(z)\right\}\begin{bmatrix}\frac{l^2E(z)}{1+\nu(z)}&0&0\\0&\frac{l^2E(z)}{1+\nu(z)}&0\\0&0&\frac{l^2E(z)}{1+\nu(z)}\end{bmatrix}dz \tag{17}$$

$$\left\{\mathcal{A}_s,\mathcal{B}_s,\mathcal{D}_s\right\}=\int_{-\frac{h}{2}}^{\frac{h}{2}}\left\{1,\mathbb{F}_{,zz}(z),\left(\mathbb{F}_{,zz}(z)\right)^2\right\}\begin{bmatrix}\frac{l^2E(z)}{1+\nu(z)}&0&0\\0&\frac{l^2E(z)}{1+\nu(z)}&0\\0&0&\frac{l^2E(z)}{1+\nu(z)}\end{bmatrix}dz$$

$$\left\{\mathcal{E}_s,\mathcal{F}_s,\mathcal{H}_s\right\}=\int_{-\frac{h}{2}}^{\frac{h}{2}}\left\{\mathbb{G}_{,z}(z),\mathbb{G}_{,z}(z)\mathbb{F}_{,zz}(z),\left(\mathbb{G}_{,z}(z)\right)^2\right\}\times\begin{bmatrix}\frac{l^2E(z)}{1+\nu(z)}&0&0\\0&\frac{l^2E(z)}{1+\nu(z)}&0\\0&0&\frac{l^2E(z)}{1+\nu(z)}\end{bmatrix}dz$$

3 Isogeometric type of numerical solving process

A finite element-based of solution methodology namely as isogeometric technique has been attracted the attention of numerus researchers. Based upon this discretizing technique for a one-dimensional problem, a knot vector having a non-decreasing feature is introduced as

$$\mathbb{K}(\xi)=\left\{\xi_1,\xi_2,\xi_3,\dots,\xi_{m+n+1}\right\} \tag{18}$$

where m is the number of B-spline basis function and n denotes the order of it. Also, each ith knot should be selected in such a way that $0\le\xi_i\le 1$.

Therefore, with the aid of the Cox-de Boor formula, the B-spline formulation of the associated basis function can be defined in recursive form as follows

$$\mathcal{X}_{i,0}(\xi)=\begin{cases}1\xi_i\le\xi<\xi_{i+1}\\0else\end{cases} \tag{19}$$

$$\mathcal{X}_{i,n}(\xi)=\left[\left(\xi-\xi_i\right)/\left(\xi_{i+n}-\xi_i\right)\right]\mathcal{X}_{i,n-1}(\xi)+\left[\left(\xi_{i+n+1}-\xi\right)/\left(\xi_{i+n+1}-\xi_{i+1}\right)\right]\mathcal{X}_{i+1,n-1}(\xi) \tag{20}$$

Accordingly, for a two-dimensional problem, the associated B-spline formulation of the basis function can be extracted via the tensor product as below

$$\mathcal{F}^{p,q}_{i,j}(\xi,\eta)=\sum_{i=1}^{m}\mathfrak{G}_i(x,y)\mathcal{P}_i \tag{21}$$

in which $\mathcal{P}_i$ stands for the ith control node within the two-directional net of control, and

$$\mathfrak{G}_i(\xi,\eta)=\mathcal{X}_{i,p}(\xi)\mathcal{X}_{j,q}(\eta)\mathfrak{W}_{i,j}/\left(\sum_{i=1}^{m}\sum_{j=1}^{n}\mathcal{X}_{i,p}(\xi)\mathcal{X}_{j,q}(\eta)\mathfrak{W}_{i,j}\right) \tag{22}$$

in which $\mathcal{X}_{i,p}(\xi)$ and $\mathcal{X}_{j,q}(\eta)$ are, respectively, the p th order and q th order shape functions associated with directions of ξ and η. Furthermore, $\mathfrak{W}_{i,j}$ represents the appropriate weight coefficient. Consequently, to carry out the derivative calculations relevant to $\mathcal{X}_{j,q}(\eta)$ shape function, the $\mathbb{K}(\eta)$ vector as a knot type of vector is put to use.

Accordingly, the isogeometric type of discretization scheme results in an accurate estimation for the components of the microplate deformation (using cubic elements as shown in Fig. 5) as follows

$$\left\{\tilde{u}^i,\tilde{v}^i,\tilde{w}^i_b,\tilde{w}^i_s\right\}^T=\sum_{i=1}^{m\times n}T_i(x,y)\begin{Bmatrix}u^i\\v^i\\w^i_b\\w^i_s\end{Bmatrix} \tag{23}$$

where

$$T_i(x,y)=\begin{bmatrix}\mathfrak{G}_i(x,y)&0&0&0\\0&\mathfrak{G}_i(x,y)&0&0\\0&0&\mathfrak{G}_i(x,y)&0\\0&0&0&\mathfrak{G}_i(x,y)\end{bmatrix} \tag{24}$$

On the basis of Eq. (6) together with Eq. (23), the components of the classical strain tensor can be discretized in the following form

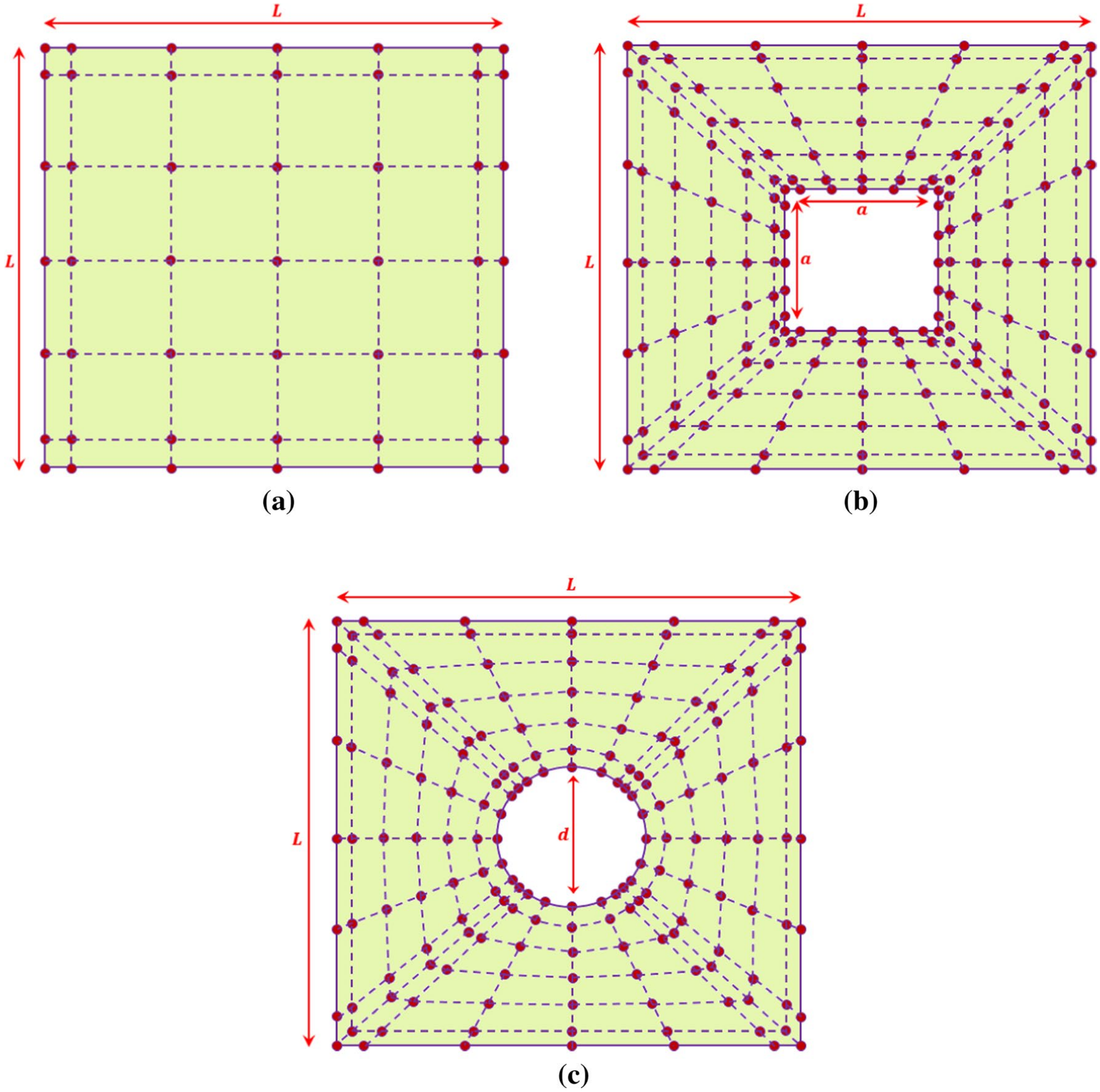

Fig. 5 Discretized square microplates with cubic elements: (a) In the absence of cutout, (b) in the presence of a square cutout, (c) in the presence of circular cutout [72]

$$\mathfrak{P}_b = \mathfrak{P}_b^L + \mathfrak{P}_b^{NL} = \sum_{i=1}^{m\times n} \mathcal{T}^i_{Lb}\mathbb{X} + \sum_{i=1}^{m\times n} \frac{1}{2}\mathcal{T}^i_{NLb}\mathbb{X}, \mathfrak{P}_s = \sum_{i=1}^{m\times n} \mathcal{T}^i_s\mathbb{X} \tag{25}$$

where

$$\mathcal{T}^i_{Lb} = \left\{ \mathcal{T}^i_{b1}\ \mathcal{T}^i_{b2}\ \mathcal{T}^i_{b3}\ \mathcal{T}^i_{b4} \right\}^T, \mathcal{T}^i_{NLb} = \left\{ \mathcal{T}^i_{b5}\ 0\ 0\ 0 \right\}^T \mathcal{T}^i_G, \mathbb{X} = \begin{Bmatrix} u^i \\ v^i \\ w^i_b \\ w^i_s \end{Bmatrix}$$

$$\mathcal{T}^i_{b1} = \begin{bmatrix} \mathfrak{G}_{i,x}(x,y) & 0 & 0\ 0 \\ 0 & \mathfrak{G}_{i,y}(x,y) & 0\ 0 \\ \mathfrak{G}_{i,y}(x,y) & \mathfrak{G}_{i,x}(x,y) & 0\ 0 \\ 0 & 0 & 0\ 0 \end{bmatrix}, \mathcal{T}^i_{b2} = -\begin{bmatrix} 0\ 0 & \mathfrak{G}_{i,xx}(x,y) & 0 \\ 0\ 0 & \mathfrak{G}_{i,yy}(x,y) & 0 \\ 0\ 0 & 2\mathfrak{G}_{i,xy}(x,y) & 0 \\ 0\ 0 & 0 & 0 \end{bmatrix}$$

$$\mathcal{T}^i_{b3} = \begin{bmatrix} 0\ 0\ 0 & \mathfrak{G}_{i,xx}(x,y) \\ 0\ 0\ 0 & \mathfrak{G}_{i,yy}(x,y) \\ 0\ 0\ 0 & 2\mathfrak{G}_{i,xy}(x,y) \\ 0\ 0\ 0 & 0 \end{bmatrix}, \mathcal{T}^i_{b4} = \begin{bmatrix} 0\ 0\ 0 & 0 \\ 0\ 0\ 0 & 0 \\ 0\ 0\ 0 & 0 \\ 0\ 0\ 0 & \mathfrak{G}_i(x,y) \end{bmatrix} \tag{26}$$

$$\mathcal{T}^{i}_{b5} = \begin{bmatrix} w_{b,x} + w_{s,x} & 0 \\ 0 & w_{b,y} + w_{s,y} \\ w_{b,y} + w_{s,y} & w_{b,x} + w_{s,x} \end{bmatrix}, \mathcal{T}^{i}_{G} = \begin{bmatrix} 0 & 0 & \mathfrak{G}_{i,x}(x,y) & \mathfrak{G}_{i,x}(x,y) \\ 0 & 0 & \mathfrak{G}_{i,y}(x,y) & \mathfrak{G}_{i,y}(x,y) \end{bmatrix}$$

Following this discretization scheme, the discretized form of the non-classical rotation gradient tensor can be written as

$$\boldsymbol{\mathfrak{R}_b} = \sum_{i=1}^{m\times n} \Vert^{i}_{b} \mathbb{X}, \boldsymbol{\mathfrak{R}_s} = \sum_{i=1}^{m\times n} \Vert^{i}_{s} \mathbb{X} \tag{27}$$

in which

$$\Vert^{i}_{b} = \left\{ \Vert^{i}_{b1} \; \Vert^{i}_{b2} \; \Vert^{i}_{b3} \right\}, \Vert^{i}_{s} = \left\{ \Vert^{i}_{s1} \; \Vert^{i}_{s2} \; \Vert^{i}_{s3} \right\} \tag{28}$$

$$\Vert^{i}_{b1} = \begin{bmatrix} 0 & 0 & \mathfrak{G}_{i,xy}(x,y) & 0 \\ 0 & 0 & -\mathfrak{G}_{i,xy}(x,y) & 0 \\ 0 & 0 & \left(\mathfrak{G}_{i,yy}(x,y) - \mathfrak{G}_{i,xx}(x,y)\right)/2 & 0 \end{bmatrix},$$

$$\Vert^{i}_{b2} = \begin{bmatrix} 0 & 0 & 0 & -\mathfrak{G}_{i,xy}(x,y)/2 \\ 0 & 0 & 0 & \mathfrak{G}_{i,xy}(x,y)/2 \\ 0 & 0 & 0 & \left(\mathfrak{G}_{i,xx}(x,y) - \mathfrak{G}_{i,yy}(x,y)\right)/4 \end{bmatrix}$$

$$\Vert^{i}_{b3} = \begin{bmatrix} 0 & 0 & 0 & \mathfrak{G}_{i,xy}(x,y)/2 \\ 0 & 0 & 0 & -\mathfrak{G}_{i,xy}(x,y)/2 \\ 0 & 0 & 0 & -\left(\mathfrak{G}_{i,xx}(x,y) - \mathfrak{G}_{i,yy}(x,y)\right)/4 \end{bmatrix},$$

$$\Vert^{i}_{s1} = \frac{1}{4} \begin{bmatrix} -\mathfrak{G}_{i,xy}(x,y) & \mathfrak{G}_{i,xx}(x,y) & 0 & 0 \\ -\mathfrak{G}_{i,yy}(x,y) & \mathfrak{G}_{i,xy}(x,y) & 0 & 0 \end{bmatrix}$$

$$\Vert^{i}_{s2} = \frac{1}{4} \begin{bmatrix} 0 & 0 & 0 & -\mathfrak{G}_{i,y}(x,y) \\ 0 & 0 & 0 & \mathfrak{G}_{i,x}(x,y) \end{bmatrix}, \Vert^{i}_{s3} = \frac{1}{4} \begin{bmatrix} 0 & 0 & 0 & \mathfrak{G}_{i,y}(x,y) \\ 0 & 0 & 0 & -\mathfrak{G}_{i,x}(x,y) \end{bmatrix}$$

As a result, the variation of the strain tensor as well as the rotation gradient tensor can be achieved as

$$\begin{aligned} \delta\left(\boldsymbol{\mathfrak{P}_b}\right) &= \delta\left(\boldsymbol{\mathfrak{P}^{L}_{b}}\right) + \delta\left(\boldsymbol{\mathfrak{P}^{NL}_{b}}\right) \\ &= \sum_{i=1}^{m\times n} \left(\mathcal{T}^{i}_{Lb} + \mathcal{T}^{i}_{NLb}\right) \begin{Bmatrix} \delta u^i \\ \delta v^i \\ \delta w^i_b \\ \delta w^i_s \end{Bmatrix}, \\ \delta\left(\boldsymbol{\mathfrak{P}_s}\right) &= \sum_{i=1}^{m\times n} \mathcal{T}^{i}_{s} \begin{Bmatrix} \delta u^i \\ \delta v^i \\ \delta w^i_b \\ \delta w^i_s \end{Bmatrix} \end{aligned}$$

$$\delta\left(\boldsymbol{\mathfrak{R}_b}\right) = \sum_{i=1}^{m\times n} \Vert^{i}_{b} \begin{Bmatrix} \delta u^i \\ \delta v^i \\ \delta w^i_b \\ \delta w^i_s \end{Bmatrix}, \delta\left(\boldsymbol{\mathfrak{R}_s}\right) = \sum_{i=1}^{m\times n} \Vert^{i}_{s} \begin{Bmatrix} \delta u^i \\ \delta v^i \\ \delta w^i_b \\ \delta w^i_s \end{Bmatrix} \tag{29}$$

Finally, by applying the introduced discretization procedure for the derived couple stress-based nonlinear differential equations, it yields

$$\mathfrak{T}(\mathbb{X})\mathbb{X} = \mathbb{p} \tag{30}$$

where the matrix of global stiffness, $\mathfrak{T}(\mathbb{X})$, can be separated to linear and nonlinear expressions as follows

$$\mathfrak{T}_L = \int_S \left\{ \left(\mathcal{T}^{i}_{Lb}\right)^{T} \xi_b \mathcal{T}^{i}_{Lb} + \left(\mathcal{T}^{i}_{s}\right)^{T} \xi_s \mathcal{T}^{i}_{s} + \left(\Vert^{i}_{b}\right)^{T} \boldsymbol{\vartheta}_b \boldsymbol{\Phi}_1 \Vert^{i}_{b} + \left(\Vert^{i}_{s}\right)^{T} \boldsymbol{\vartheta}_s \Vert^{i}_{s} \right\} dS \tag{31a}$$

$$\mathfrak{T}_{NL}(\mathbb{X}) = \int_S \left\{ \frac{1}{2}\left(\mathcal{T}^{i}_{Lb}\right)^{T} \xi_b \mathcal{T}^{i}_{NLb} + \left(\mathcal{T}^{i}_{NLb}\right)^{T} \xi_b \mathcal{T}^{i}_{Lb} + \frac{1}{2}\left(\mathcal{T}^{i}_{NLb}\right)^{T} \xi_b \mathcal{T}^{i}_{NLb} \right\} dS \tag{31b}$$

On the hand, to express the load vector, one will have

$$\mathbb{p} = \int_S \Pi \begin{Bmatrix} 0 \\ 0 \\ \mathfrak{G}_i(x,y) \\ \mathfrak{G}_i(x,y) \end{Bmatrix} dS \tag{32}$$

Now, to apply the Newton–Raphson kind of iterative solving process to Eq. (30), the vector of residual force is defined in the following form

$$\mathcal{R}(\mathbb{X}) = \mathfrak{T}(\mathbb{X})\mathbb{X} - \mathbb{p} = \left[\mathfrak{T}_L + \mathfrak{T}_{NL}(\mathbb{X})\right]\mathbb{X} - \mathbb{p} \tag{33}$$

To continue the associated iteration, an incremental form for the microplate deformation is taken into account as

$$\Delta\mathbb{X} = -\frac{\mathcal{R}\left(\mathbb{X}^i\right)}{\left(\mathfrak{T}_L + \mathfrak{T}_{NL} + \mathfrak{T}_G\right)} \tag{34}$$

where

$$\mathbb{X}^{i+1} = \mathbb{X}^i + \Delta\mathbb{X} \tag{35}$$

and the matrix of geometric stiffness, $\mathfrak{T}_G$, can be written as below

$$\mathfrak{T}_G = \int_S \left\{ \left(\mathcal{T}_{G1}\right)^{T} \boldsymbol{N_x} \mathcal{T}_{G1} + \left(\mathcal{T}_{G2}\right)^{T} \boldsymbol{N_y} \mathcal{T}_{G2} \right\} dS \tag{36}$$

in which

$$\mathcal{T}_{G1} = \begin{bmatrix} 0 & 0 & \mathfrak{G}_{i,x}(x,y) & 0 \\ 0 & 0 & \mathfrak{G}_{i,y}(x,y) & 0 \end{bmatrix}, \mathcal{T}_{G2} = \begin{bmatrix} 0 & 0 & 0 & \mathfrak{G}_{i,x}(x,y) \\ 0 & 0 & 0 & \mathfrak{G}_{i,y}(x,y) \end{bmatrix} \tag{37}$$

and $\boldsymbol{N_x}$, $\boldsymbol{N_y}$ denote, respectively, the force-type resultants in x-axis and y-axis directions.

4 Numerical results and discussion

Herein, the non-dimensional couple stress elasticity-based porosity- and size-dependent nonlinear bending characteristics of the porous FG composite microplates under external uniform distributed load. The results are

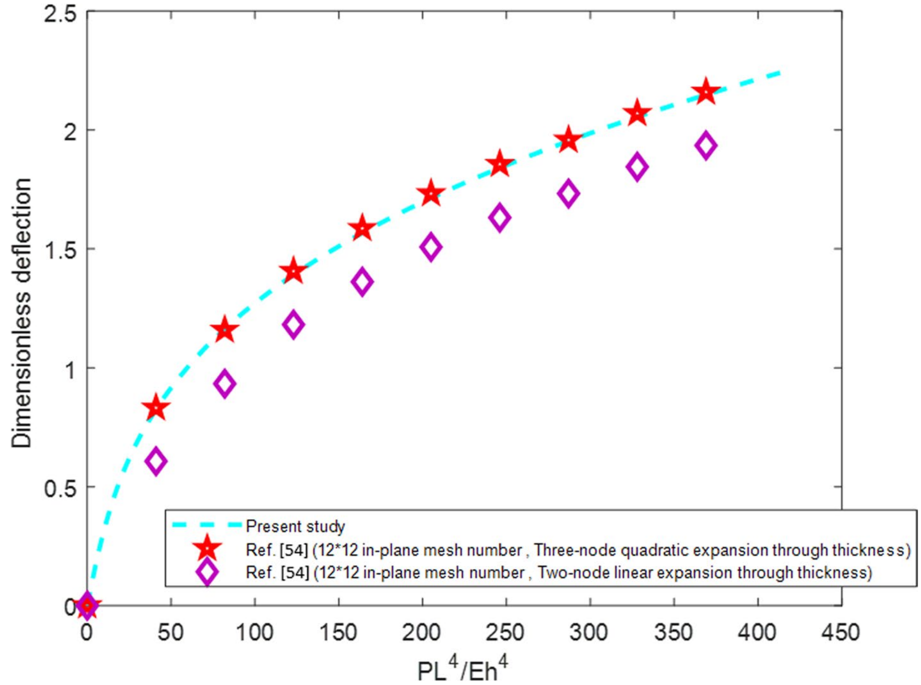

Fig. 6 Comparison study on the nonlinear bending behavior of a square plate at macro-scale subjected to a uniform distributed load and simply supported boundary conditions ($h/L = 0.1$)

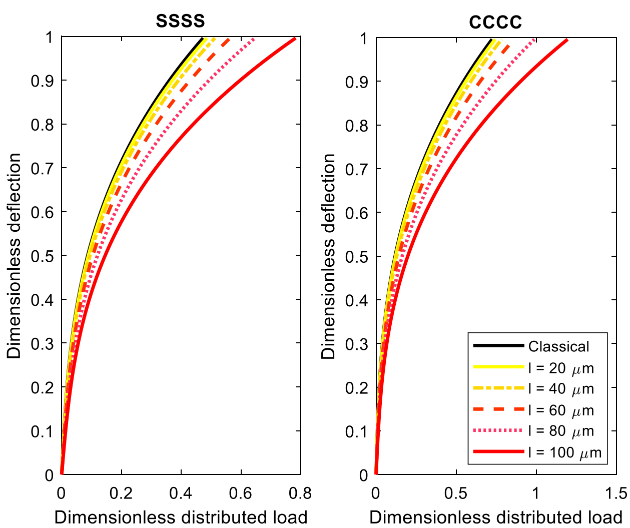

Fig. 7 Classical and couple stress-based nonlinear flexural response of porous FG composite microplates corresponding to different internal length scale parameters ($\Gamma = 0.4$, $k = 0.5$, $a/L = d/L = 0$, U-PFGM pattern)

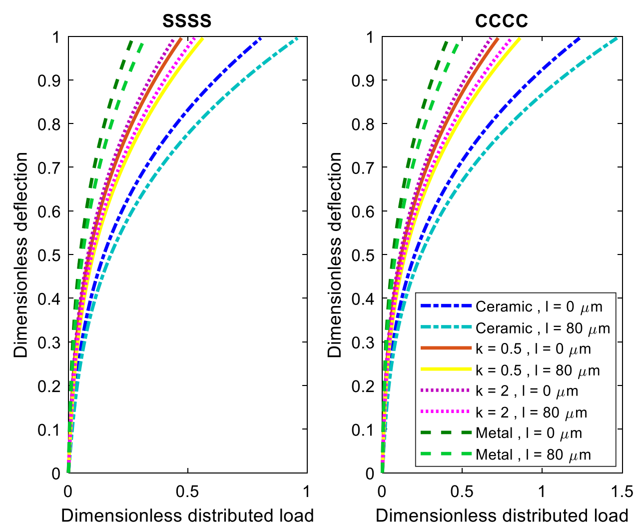

Fig. 8 Classical and couple stress-based nonlinear flexural response of porous FG composite microplates corresponding to different material gradient indexes. ($\Gamma = 0.4$, $a/L = d/L = 0$, U-PFGM pattern)

presented in the presence and absence of a cutout with various shapes located at the center of microplates. The material gradient of porous FG composite microplates is supposed in such a way to make a ceramic-rich top surface and a metal-rich bottom surface, having the properties of: $E_c = 210GPa$, $\nu = 0.24$ associated with the ceramic component, $E_m = 70GPa$, $\nu = 0.35$ associated with the metal component [53]. In addition, the dimensionless distributed load and plate deflection are defined as $\overline{P} = PL_1^2/E_m h^3$, $W = w/h$. Also, the geometric of rectangular microplates is selected as $h = 20\mu m, L_1 = 50h, L_1/L_2 = 1$.

At the beginning, the proposed solving procedure is validated. In accordance with this purpose, the terms associated with the small-scale effect are ignored, and then the nonlinear bending behavior of a homogenous plate at macroscale is achieved and compared with that reported previously by Wu et al. [54] using Carrera unified formulation (CUF). The comparison study is made with the both two-node linear and three-node quadratic of expansion functions through the plate thickness. As displayed in Fig. 6, the matched results confirm the accuracy and correction of the introduced quasi-3D plate model as well as numerical solution methodology.

In Fig. 7, the classical and couple-stress-based nonlinear flexural curves of porous FG composite microplates in the absence of a central cutout are illustrated corresponding to different internal length scale parameters and edge supports. By comparing the couple stress-based curves with the classical counterparts, it can be reached to this point that the role of couple stress size dependency incorporating an extra stiffness due to deriving the gradient of rotation leads to decrease the maximum deflection of the microplate under a specific value of uniform load which confirms the stiffening manner of it. The obtained tendency is repeated for the both types of the considered plate edge supports including fully clamped (CCCC) and fully simply supported (SSSS).

Figure 8 depicts the classical and couple stress-based nonlinear flexural curves of porous FG composite microplates in the absence of a central cutout relevant to various values of the material gradient index. It is found that by changing the properties from the full ceramic component to the full metal one, a significant reduction in the slope of the nonlinear flexural response occurs. Moreover, the difference between the classical and couple stress-based obtained plots gets larger by moving from microplate made of the full metal components to that made of full ceramic one.

The nonlinear flexural feature of porous FG composite microplates in the absence of a central located cutout is displayed in Fig. 9 relevant to various through-thickness porosity distribution schemes. It is observed that the gap

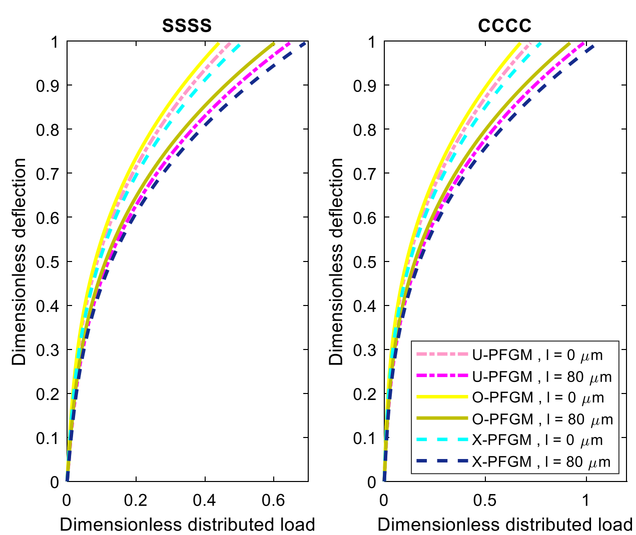

Fig. 9 Classical and couple stress-based nonlinear flexural behavior of porous FG composite microplates corresponding to different through-thickness porosity distribution schemes ($\Gamma = 0.4$, $k = 0.5$, $a/L = d/L = 0$)

Table 1 Classical and couple stress-based dimensionless distributed loads of porous FG composite microplates relevant to different material gradient indexes ($\Gamma = 0.4$)

k	$l(\mu m)$	U-PFGM	O-PFGM	X-PFGM
SSSS boundary conditions				
0.5	$w/h = 0.4$			
	0	0.0553	0.0515	0.0591
	40	0.0600 (+8.56%)	0.0559 (+8.56%)	0.0642 (+8.56%)
	80	0.0761 (+37.63%)	0.0708 (+37.63%)	0.0813 (+37.63%)
	$w/h = 0.8$			
	0	0.2662	0.2478	0.2846
	40	0.2885 (+8.37%)	0.2685 (+8.37%)	0.3084 (+8.37%)
	80	0.3640 (+36.76%)	0.3389 (+36.76%)	0.3892 (+36.76%)
2	$w/h = 0.4$			
	0	0.0518	0.0483	0.0554
	40	0.0563 (+8.61%)	0.0524 (+8.61%)	0.0602 (+8.61%)
	80	0.0714 (+37.85%)	0.0664 (+37.85%)	0.0763 (+37.85%)
	$w/h = 0.8$			
	0	0.2496	0.2324	0.2669
	40	0.2705 (+8.42%)	0.2518 (+8.42%)	0.2892 (+8.42%)
	80	0.3414 (+36.98%)	0.3178 (+36.98%)	0.3650 (+36.98%)
CCCC boundary conditions				
0.5	$w/h = 0.4$			
	0	0.0715	0.0666	0.0765
	40	0.0776 (+8.49%)	0.0722 (+8.49%)	0.0830 (+8.49%)
	80	0.0982 (+37.29%)	0.0914 (+37.29%)	0.1050 (+37.29%)
	$w/h = 0.8$			
	0	0.3961	0.3687	0.4234
	40	0.4290 (+8.33%)	0.3994 (+8.33%)	0.4587 (+8.33%)
	80	0.5409 (+36.56%)	0.5035 (+36.56%)	0.5782 (+36.56%)
2	$w/h = 0.4$			
	0	0.0671	0.0624	0.0717
	40	0.0728 (+8.53%)	0.0677 (+8.53%)	0.0778 (+8.53%)
	80	0.0921 (+37.46%)	0.0857 (+37.46%)	0.0985 (+37.46%)
	$w/h = 0.8$			
	0	0.3714	0.3458	0.3971
	40	0.4024 (+8.36%)	0.3746 (+8.36%)	0.4302 (+8.36%)
	80	0.5072 (+36.71%)	0.4722 (+36.71%)	0.5423 (+36.71%)

between nonlinear flexural responses associated with different porosity patterns is somehow higher by considering the couple stress size effect. Furthermore, this observation is repeated for all dispersion schemes, and both types of plate edge supports.

Table 2 Classical and couple stress-based dimensionless distributed loads of porous FG composite microplates relevant to different porosity indexes ($k = 2$)

Γ	l (μm)	U-PFGM	O-PFGM	X-PFGM
SSSS boundary conditions				
0.3	$w/h = 0.4$			
	0	0.0587	0.0559	0.0616
	40	0.0638 (+8.56%)	0.0607 (+8.56%)	0.0669 (+8.56%)
	80	0.0808 (+37.63%)	0.0769 (+37.63%)	0.0848 (+37.63%)
	$w/h = 0.8$			
	0	0.2828	0.2690	0.2966
	40	0.3065 (+8.37%)	0.2915 (+8.37%)	0.3214 (+8.37%)
	80	0.3868 (+36.76%)	0.3679 (+36.77%)	0.4057 (+36.77%)
0.5	$w/h = 0.4$			
	0	0.0518	0.0471	0.0566
	40	0.0563 (+8.56%)	0.0511 (+8.56%)	0.0615 (+8.56%)
	80	0.0713 (+37.62%)	0.0648 (+37.63%)	0.0779 (+37.63%)
	$w/h = 0.8$			
	0	0.2495	0.2265	0.2725
	40	0.2704 (+8.37%)	0.2455 (+8.37%)	0.2954 (+8.37%)
	80	0.3413 (+36.76%)	0.3098 (+36.76%)	0.3727 (+36.77%)
CCCC boundary conditions				
0.3	$w/h = 0.4$			
	0	0.0760	0.0723	0.0797
	40	0.0824 (+8.49%)	0.0784 (+8.49%)	0.0865 (+8.49%)
	80	0.1043 (+37.29%)	0.0992 (+37.29%)	0.1094 (+37.29%)
	$w/h = 0.8$			
	0	0.4208	0.4003	0.4413
	40	0.4559 (+8.33%)	0.4336 (+8.33%)	0.4781 (+8.33%)
	80	0.5747 (+36.56%)	0.5466 (+36.56%)	0.6027 (+36.56%)
0.5	$w/h = 0.4$			
	0	0.0670	0.0609	0.0732
	40	0.0727 (+8.49%)	0.0660 (+8.49%)	0.0794 (+8.49%)
	80	0.0921 (+37.29%)	0.0836 (+37.29%)	0.1005 (+37.29%)
	$w/h = 0.8$			
	0	0.3713	0.3371	0.4055
	40	0.4022 (+8.33%)	0.3652 (+8.33%)	0.4393 (+8.33%)
	80	0.5071 (+36.56%)	0.4603 (+36.56%)	0.5538 (+36.56%)

Tables 1 and 2 give the classical and couple stress-based applied uniform loads relevant to various porosity and material gradient indexes, respectively, as well as a specific value of the porous FG composite microplate deflection in the absence of a central cutout. The significance

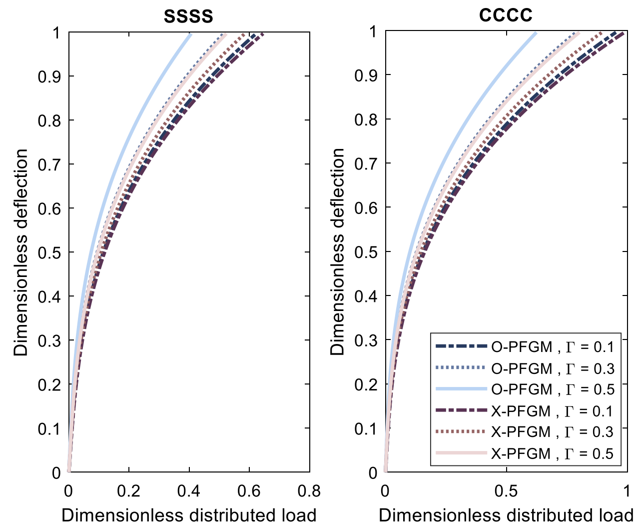

Fig. 10 Couple stress-based nonlinear flexural behavior of porous FG composite microplates corresponding to different porosity indexes ($l = 60\mu m$, $k = 0.5$, $a/L = d/L = 0$)

of the small scale effect is indicated by the percentages written in parentheses. It is found that by inducing a higher deformation, the role of the couple stress size effect becomes less essential. This anticipation is repeated for all material gradient and porosity indexes. Additionally, it is seen that for all induced plate deformation, the couple stress size effect on the necessary applied load is somehow more considerable for a simply supported porous FG composite microplate than a clamped one. Among different schemes of the through-thickness porosity distribution,

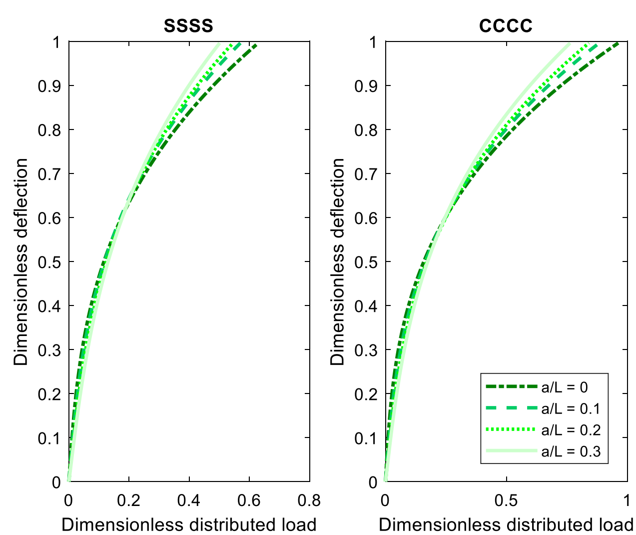

Fig. 11 Role of existence a central located square cutout in the couple stress-based nonlinear flexural behavior of porous FG composite microplates ($l = 60\mu m$, $\Gamma = 0.4$, $k = 0.5$, U-PFGM pattern)

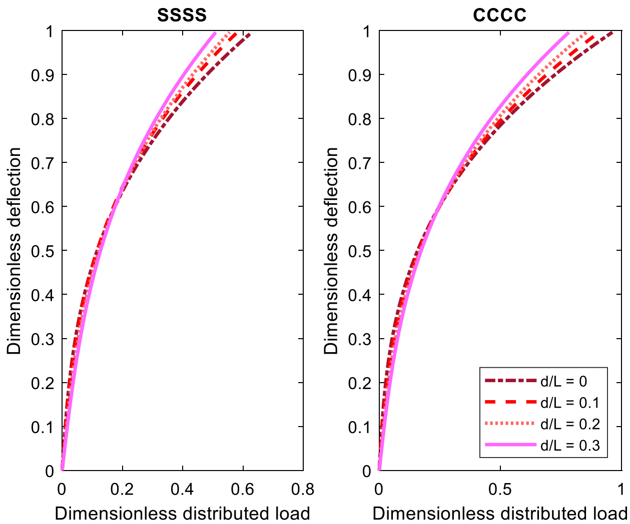

Fig. 12 Role of existence a central located circular cutout in the couple stress-based nonlinear flexural behavior of porous FG composite microplates ($l = 60\mu m$, $\Gamma = 0.4$, $k = 0.5$, U-PFGM pattern)

the O-PFGM and X-PFGM microplates have, respectively, the minimum and maximum nonlinear flexural stiffness.

In Fig. 10, the couple stress-based nonlinear flexural behaviors of porous FG composite microplates having O-PFGM and X-PFGM schemes and in the absence of a central cutout are highlighted relevant to different porosity indexes. It can be found by considering a higher porosity index for a porous FG composite microplate, an increment occurs in the difference between couple stress-based nonlinear flexural responses of microplates having O-PFGM and X-PFGM through-thickness porosity schemes.

The role of existence a cutout having various shapes located at the center of porous FG composite microplate in the couple stress-based nonlinear flexural response of it is represented in Figs. 11 and 12. So, the nonlinear flexural plats of porous FG composite microplates having, respectively, square and circular cutouts located at their center are shown. It can be found the tendency and slope of the nonlinear flexural response can be changed in the presence of a central cutout. In accordance with this point, the existence of a central cutout results in to achieve a specific value of the external uniform load, corresponding to which the predicted shift of tendency occurs. The cutout geometry parameters as well as the type of edge supports play important role in the value of this extracted applied load. This behavior may be related to this fact that for very small applied load and associated induced deflection, the supports of cutout edges at the center of microplate plays the prominent role in the bending stiffness which cause to enhance it. However, by increasing the applied load and the induced deflection, the influence of the reduced stiffness due to the existing a central cutout in the plate geometry becomes more important.

Table 3 Role of the existence a central located cutout on the couple stress-based nonlinear flexural response of U-PFGM square microplates with SSSS boundary conditions ($k = 0.5, \Gamma = 0.4$)

l (μm)	a/L	Dimensionless load	d/L	Dimensionless load
40	$w/h = 0.4$			
	0	0.0600	0	0.0600
	0.1	0.0638 (+6.40%)	0.1	0.0617 (+2.92%)
	0.2	0.0695 (+15.84%)	0.2	0.0673 (+12.28%)
	0.3	0.0749 (+24.91%)	0.3	0.0727 (+21.19%)
	$w/h = 0.8$			
	0	0.2885	0	0.2885
	0.1	0.2688 (– 6.65%)	0.1	0.2713 (– 5.79%)
	0.2	0.2642 (– 8.22%)	0.2	0.2663 (– 7.50%)
	0.3	0.2521 (– 12.43%)	0.3	0.2534 (– 11.97%)
80	$w/h = 0.4$			
	0	0.0761	0	0.0761
	0.1	0.0810 (+6.54%)	0.1	0.0783 (+3.01%)
	0.2	0.0883 (+16.10%)	0.2	0.0856 (+12.49%)
	0.3	0.0953 (+25.31%)	0.3	0.0924 (+21.54%)
	$w/h = 0.8$			
	0	0..3640	0	0.3640
	0.1	0.3399 (– 6.55%)	0.1	0.3429 (– 5.72%)
	0.2	0.3345 (– 8.04%)	0.2	0.3370 (– 7.36%)
	0.3	0.3195 (– 12.15%)	0.3	0.3211 (– 11.73%)

Table 4 Role of the existence a central located cutout on the couple stress-based nonlinear flexural response of U-PFGM square microplates with CCCC boundary conditions ($k = 0.5, \Gamma = 0.4$)

l (μm)	a/L	Dimensionless load	d/L	Dimensionless load
40	$w/h = 0.4$			
	0	0.0776	0	0.0776
	0.1	0.0849 (+9.51%)	0.1	0.0835 (+7.71%)
	0.2	0.0912 (+17.66%)	0.2	0.0893 (+15.20%)
	0.3	0.0967 (+24.82%)	0.3	0.0951 (+22.71%)
	$w/h = 0.8$			
	0	0.4290	0	0.4290
	0.1	0.4047 (– 5.47%)	0.1	0.4127 (– 3.61%)
	0.2	0.3939 (– 8.01%)	0.2	0.3978 (– 7.09%)
	0.3	0.3693 (– 13.76%)	0.3	0.3754 (– 12.33%)
80	$w/h = 0.4$			
	0	0.0982	0	0.0982
	0.1	0.1076 (+9.69%)	0.1	0.1058 (+7.85%)
	0.2	0.1158 (+17.97%)	0.2	0.1133 (+15.47%)
	0.3	0.1230 (+25.29%)	0.3	0.1208 (+23.14%)
	$w/h = 0.8$			
	0	0.5115	0	0.5409
	0.1	0.4594 (– 5.38%)	0.1	0.5213 (– 3.53%)
	0.2	0.4361 (– 7.84%)	0.2	0.5029 (– 6.94%)
	0.3	0.3962 (– 13.51%)	0.3	0.4750 (– 12.11%)

In Tables 3 and 4, the couple stress-based applied uniform loads corresponding to specific values of the porous FG composite microplate deflection in the presence of, respectively, square and circular central cutouts are presented for CCCC and SSSS edge supports. The percentages written in parentheses stand for the gap between the distributed loads in the presence of a central cutout and its counterpart in the absence of it. The change in the trend of load–deflection response due to a central cutout is obvious again, as for a lower plate deflection, the presence of a cutout causes to increase the dimensionless load, while by moving to deeper region of the bending response, it results in to decrease the bending stiffness. It can be found that the reduction in the bending stiffness of a porous FG composite microplate due to the existence of a square central located cutout is higher than that of a circular one with the same aspect ratio ($a/L = d/L$). This anticipation is similar for different small scale parameter as well as various boundary conditions. In addition, it is observed that by changing the edge supports from SSSS type to CCCC one, the influence of a central cutout on the reduction of the couple stress-based bending stiffness of a microplate decreases.

5 Concluding remarks

In the current work, in the context of a new quasi-3D plate theory together with the modified couple stress continuum mechanics, the porosity- and size-dependent nonlinear flexural response of porous FG composite microplates in the presence and absence of a cutout with various shapes located at their center was investigated. A numerical solution methodology based upon the isogeometric finite element approach was employed to fulfill effectively the higher continuity requirements.

It was deduced that the role of couple stress size dependency incorporating an extra stiffness due to deriving the gradient of rotation leads to decrease the maximum deflection of the microplate under a specific value of uniform load. It was found that by inducing a higher deformation, the role of the couple stress size effect becomes less essential. This anticipation is repeated for all material gradient and porosity indexes. In addition, it was pointed out that among different schemes of the through-thickness porosity distribution, the O-PFGM and X-PFGM microplates have, respectively, the minimum and maximum nonlinear flexural stiffness. Moreover, it was observed that the tendency and slope of the nonlinear flexural response can be changed in the presence of a central cutout. In accordance with this point, the existence of a central cutout results in to achieve a specific value of the external uniform load, corresponding to which the predicted shift of tendency occurs. It was seen that the reduction in the bending stiffness of a porous FG composite microplate due to a square central located cutout is higher than that of a circular one with the same aspect ratio. In addition, it was revealed that the reduction in the bending stiffness of a porous FG composite microplate due to the existence of a square central located cutout is a bit higher than that of a circular central cutout with the same aspect ratio ($a/L = d/L$).

Declarations

Conflict of interest All authors declare that they have no conflict of interest.

References

1. Cheng H, Li L, Wang B, Feng X, Mao Z, Vancso GJ, Sui X. Multifaceted applications of cellulosic porous materials in environment, energy, and health. Progr Polym Sci. 2020;106:101253.
2. Wang H, Liu X, Niu P, Wang S, Shi J, Li L. Porous two-dimensional materials for photocatalytic and electrocatalytic applications. Matter. 2020;2:1377–413.
3. Ansari SA, Parveen N, Mahfoz Kotb H, Alshoaibi A. Hydrothermally derived three-dimensional porous hollow double-walled Mn_2O_3 nanocubes as superior electrode materials for supercapacitor applications. Electrochim Acta. 2020;355:136783.
4. Zhang W, Bao Y, Bao A. Preparation of nitrogen-doped hierarchical porous carbon materials by a template-free method and application to CO_2 capture. J Environ Chem Eng. 2020;8:103732.
5. Yu K, Wang J, Wang X, Liang J, Liang C. Sustainable application of biomass by-products: corn straw-derived porous carbon nanospheres using as anode materials for lithium ion batteries. Mater Chem Phys. 2020;243:122644.
6. Lin J, Cai X, Liu Z, Liu N, Xie M, et al. Anti-liquid-interfering and bacterially antiadhve strategy for highly stretchable and ultrasensitive strain sensors based on cassie-baxter wetting state. Adv Func Mater. 2020. https://doi.org/10.1002/adfm.202000398.
7. Ansari R, Sahmani S. Nonlocal beam models for buckling of nanobeams using state-space method regarding different boundary conditions. J Mech Sci Technol. 2011;25:2365.
8. Sahmani S, Bahrami M, Ansari R. Surface energy effects on the free vibration characteristics of postbuckled third-order shear deformable nanobeams. Compos Struct. 2014;116:552–61.
9. Reddy JN, Romanoff J, Loya JA. Nonlinear finite element analysis of functionally graded circular plates with modified couple stress theory. Eur J Mech. 2016;56:92–104.
10. Togun N, Bagdatli SM. Size dependent nonlinear vibration of the tensioned nanobeam based on the modified couple stress theory. Compos B Eng. 2016;97:255–62.
11. Lou J, He L, Du J, Wu H. Buckling and post-buckling analyses of piezoelectric hybrid microplates subject to thermo–electro-mechanical loads based on the modified couple stress theory. Compos Struct. 2016;153:332–44.
12. Sahmani S, Aghdam MM, Bahrami M. Surface free energy effects on the postbuckling behavior of cylindrical shear deformable nanoshells under combined axial and radial compressions. Meccanica. 2017;52:1329–52.
13. Malikan M. Electro-mechanical shear buckling of piezoelectric nanoplate using modified couple stress theory based on

simplified first order shear deformation theory. Appl Math Model. 2017;48:196–207.
14. Safaei B, Fattahi AM. Free vibrational response of single-layered graphene sheets embedded in an elastic matrix using different nonlocal plate models. Mechanics. 2017;23:678–87.
15. She G-L, Yuan F-G, Ren Y-R. Nonlinear analysis of bending, thermal buckling and post-buckling for functionally graded tubes by using a refined beam theory. Compos Struct. 2017;165:74–82.
16. Sahmani S, Aghdam MM. Size-dependent nonlinear bending of micro/nano-beams made of nanoporous biomaterials including a refined truncated cube cell. Phys Lett A. 2017;381:3818–30.
17. Sahmani S, Aghdam MM. Nonlinear primary resonance of micro/nano-beams made of nanoporous biomaterials incorporating nonlocality and strain gradient size dependency. Results Phys. 2018;8:879–92.
18. Arefi M, Bidgoli EMR, Dimitri R, Tornabene F. Free vibrations of functionally graded polymer composite nanoplates reinforced with graphene nanoplatelets. Aerosp Sci Technol. 2018;81:108–17.
19. Sahmani S, Fattahi AM. Small scale effects on buckling and postbuckling behaviors of axially loaded FGM nanoshells based on nonlocal strain gradient elasticity theory. Appl Math Mech. 2018;39:561–80.
20. Soleimani I, Tadi Beni Y. Vibration analysis of nanotubes based on two-node size-dependent axisymmetric shell element. Arch Civil Mech Eng. 2018;18:1345–58.
21. Sahmani S, Aghdam MM, Rabczuk T. Nonlinear bending of functionally graded porous micro/nano-beams reinforced with graphene platelets based upon nonlocal strain gradient theory. Compos Struct. 2018;186:68–78.
22. Li X, Li L, Hu Y, Ding Z, Deng W. Sustainable application of biomass by-products: Corn straw-derived porous carbon nanospheres using as anode materials for lithium ion batteries. Compos Struct. 2017;165:250–65.
23. Sahmani S, Aghdam MM. Imperfection sensitivity of the size-dependent postbuckling response of pressurized FGM nanoshells in thermal environments. Arch Civil Mech Eng. 2017;17:623–38.
24. Joshi PV, Gupta A, Jain NK, Salhotra R, Rawani AM, Ramtekkar GD. Effect of thermal environment on free vibration and buckling of partially cracked isotropic and FGM micro plates based on a non classical Kirchhoff's plate theory: an analytical approach. Int J Mech Sci. 2017;131:155–70.
25. Radic N, Jeremic D. A comprehensive study on vibration and buckling of orthotropic double-layered graphene sheets under hygrothermal loading with different boundary conditions. Compos B Eng. 2017;128:182–99.
26. Sahmani S, Aghdam MM. Size-dependent axial instability of microtubules surrounded by cytoplasm of a living cell based on nonlocal strain gradient elasticity theory. J Theor Biol. 2017;422:59–71.
27. Khakalo S, Balobanov V, Niiranen J. Modelling size-dependent bending, buckling and vibrations of 2D triangular lattices by strain gradient elasticity models: applications to sandwich beams and auxetics. Int J Eng Sci. 2018;127:33–52.
28. Al-Shujairi M, Mollamahmutoglu C. Buckling and free vibration analysis of functionally graded sandwich micro-beams resting on elastic foundation by using nonlocal strain gradient theory in conjunction with higher order shear theories under thermal effect. Compos B Eng. 2018;154:292–312.
29. Ruocco E, Zhang H, Wang CM. Buckling and vibration analysis of nonlocal axially functionally graded nanobeams based on Hencky-bar chain model. Appl Math Model. 2018;63:445–63.
30. Jia XL, Ke LL, Zhong XL, Sun Y, Yang J, Kitipornchai S. Thermal-mechanical-electrical buckling behavior of functionally graded micro-beams based on modified couple stress theory. Compos Struct. 2018;202:625–34.
31. Taati E. On buckling and post-buckling behavior of functionally graded micro-beams in thermal environment. Int J Eng Sci. 2018;128:63–78.
32. Ghorbani Shenas A, Ziaee S, Malekzadeh P. Post-buckling and vibration of post-buckled rotating pre-twisted FG microbeams in thermal environment. Thin-Walled Struct. 2019;138:335–60.
33. Sarafraz A, Sahmani S, Aghdam MM. Nonlinear secondary resonance of nanobeams under subharmonic and superharmonic excitations including surface free energy effects. Appl Math Model. 2019;66:195–226.
34. Aria AI, Friswell MI. Computational hygro-thermal vibration and buckling analysis of functionally graded sandwich microbeams. Compos B Eng. 2019;165:785–97.
35. Yu YJ, Zhang K, Deng ZC. Buckling analyses of three characteristic-lengths featured size-dependent gradient-beam with variational consistent higher order boundary conditions. Appl Math Model. 2019;74:1–20.
36. Thai CH, Ferreira AJM, Phung-Van P. Size dependent free vibration analysis of multilayer functionally graded GPLRC microplates based on modified strain gradient theory. Compos B Eng. 2019;169:174–88.
37. Sahmani S, Safaei B. Nonlocal strain gradient nonlinear resonance of bi-directional functionally graded composite micro/nano-beams under periodic soft excitation. Thin-Walled Struct . 2019;143:106226.
38. Fang J, Zheng S, Xiao J, Zhang X. Vibration and thermal buckling analysis of rotating nonlocal functionally graded nanobeams in thermal environment. Aerospace Sci Technol. 2020;106:106146.
39. Sarthak D, Prateek G, Vasudevan R, Polit O, Ganapathi M. Dynamic buckling of classical/non-classical curved beams by nonlocal nonlinear finite element accounting for size dependent effect and using higher-order shear flexible model. Int J Non-Linear Mech. 2020;125:103536.
40. Yuan Y, Zhao K, Zhao Y, Sahmani S, Safaie B. Couple stress-based nonlinear buckling analysis of hydrostatic pressurized functionally graded composite conical microshells. Mech Mater. 2020;148:103507.
41. Thai CH, Tran TD, Phung-Van P. A size-dependent moving Kriging meshfree model for deformation and free vibration analysis of functionally graded carbon nanotube-reinforced composite nanoplates. Eng Anal Boundary Elem. 2020;115:52–63.
42. Yuan Y, Zhao K, Sahmani S, Safaei B. Size-dependent shear buckling response of FGM skew nanoplates modeled via different homogenization schemes. Appl Math Mech. 2020;41:587–604.
43. Fan F, Lei B, Sahmani S, Safaei B. On the surface elastic-based shear buckling characteristics of functionally graded composite skew nanoplates. Thin-Walled Struct. 2020;154:106841.
44. Zhang B, Li H, Kong L, Shen H, Zhang Z. Size-dependent static and dynamic analysis of Reddy-type micro-beams by strain gradient differential quadrature finite element method. Thin-Walled Struct. 2020;148:106496.
45. Daghigh H, Daghigh V, Milani A, Tannant D, Lacy TE Jr, Reddy JN. Nonlocal bending and buckling of agglomerated CNT-Reinforced composite nanoplates. Compos B. 2020;183:107716.
46. Karamanli A, Vo TP. Size-dependent behaviour of functionally graded sandwich microbeams based on the modified strain gradient theory. Compos Struct. 2020;246:112401.
47. Guo J, Sun T, Pan E. Three-dimensional nonlocal buckling of composite nanoplates with coated one-dimensional quasicrystal in an elastic medium. Int J Solids Struct. 2020;185:272–80.
48. Mao JJ, Lu HM, Zhang W, Lai SK. Vibrations of graphene nanoplatelet reinforced functionally gradient piezoelectric composite microplate based on nonlocal theory. Compos Struct. 2020;236:111813.
49. Fan F, Xu Y, Sahmani S, Safaei B. Modified couple stress-based geometrically nonlinear oscillations of porous functionally graded

microplates using NURBS-based isogeometric approach. Comput Methods Appl Mech Engi. 2020;372:113400.
50. Sahmani S, Safaei B. Large-amplitude oscillations of composite conical nanoshells with in-plane heterogeneity including surface stress effect. Appl Math Model. 2021;89:1792–813.
51. Phung-Van P, Thai CH, Nguyen-Xuan H, Abdel-Wahab M. An isogeometric approach of static and free vibration analyses for porous FG nanoplates. Eur J Mech. 2019;78:103851.
52. Tsaitas GC. A new Kirchhoff plate model based on a modified couple stress theory. Int J Solids Struct. 2009;46:2757–64.
53. Miller RE, Shenoy VB. Size-dependent elastic properties of nanosized structural elements. Nanotechnology. 2000;11:139–47.
54. Wu B, Pagani A, Filippi M, Chen WQ, Carrera E. Large-deflection and post-buckling analyses of isotropic rectangular plates by Carrera Unified Formulation. Int J Non-Linear Mech. 2019;116:18–31.